

# Automated image acquisition and processing using a new generation of 4K × 4K CCD cameras for cryo electron microscopic studies of macromolecular assemblies

Peijun Zhang,<sup>a</sup> Mario J. Borgnia,<sup>b</sup> Paul Mooney,<sup>c</sup> Dan Shi,<sup>a</sup> Ming Pan,<sup>c</sup> Philip O'Herron,<sup>b</sup> Albert Mao,<sup>a</sup> David Brogan,<sup>a</sup> Jacqueline L.S. Milne,<sup>b</sup> and Sriram Subramaniam<sup>a,\*</sup>

<sup>a</sup> Laboratory of Biochemistry, National Cancer Institute, National Institutes of Health, Bethesda, MD 20892, USA

<sup>b</sup> Laboratory of Cell Biology, National Cancer Institute, National Institutes of Health, Bethesda, MD 20892, USA

<sup>c</sup> GATAN Inc., Pleasanton, CA, USA

Received 25 February 2003, and in revised form 12 June 2003

## Abstract

We have previously reported the development of AutoEM, a software package for semi-automated acquisition of data from a transmission electron microscope. In continuing efforts to improve the speed of structure determination of macromolecular assemblies by electron microscopy, we report here on the performance of a new generation of 4K CCD cameras for use in cryo electron microscopic applications. We demonstrate that at 120 kV, and at a nominal magnification of 67 000×, power spectra and signal-to-noise ratios for the new 4K CCD camera are comparable to values obtained for film images scanned using a Zeiss scanner to resolutions as high as  $\sim 1/6.5 \text{ \AA}^{-1}$ . The specimen area imaged for each exposure on the 4K CCD is about one-third of the area that can be recorded with a similar exposure on film. The CCD camera also serves the purpose of recording images at low magnification from the center of the hole to measure the thickness of vitrified ice in the hole. The performance of the camera is satisfactory under the low-dose conditions used in cryo electron microscopy, as demonstrated here by the determination of a three-dimensional map at 15 Å for the catalytic core of the 1.8 MDa *Bacillus stearothermophilus* icosahedral pyruvate dehydrogenase complex, and its comparison with the previously reported atomic model for this complex obtained by X-ray crystallography.

Published by Elsevier Inc.

**Keywords:** Cryo electron microscopy; CCD camera; Image processing

## 1. Introduction

Cryo electron microscopy using the “single particle” approach is rapidly emerging as a powerful tool for the analysis of the structures of large macromolecular complexes that are not easily amenable to investigation by either X-ray crystallographic or NMR approaches (Conway et al., 2001; Frank, 1996; Jiang et al., 2003; Milne et al., 2002; Ranson et al., 2001; Stark et al., 2000). The experimental aspects of this approach to structure determination typically involve: (i) preparation of a frozen hydrated specimen from a chemically and structurally homogeneous preparation of the macro-

molecular complex, (ii) identification of the regions of the specimen with optimal particle densities and vitreous ice thickness that are most likely to produce the best images, (iii) recording of a large number of images from such regions of the specimen using optimal settings for imaging parameters such as defocus values, magnification and electron dose, (iv) “boxing” regions of the image representing projection views of individual molecular complexes using manual or semi-automated approaches, (v) combining the individual images to derive a three-dimensional model for the complex by computing the relative orientations of the various images with respect to each other and finally, (vi) positioning into the density the atomic co-ordinates of those sub-components of the complex for which structures may be available from crystallographic or NMR studies. For

\* Corresponding author. Fax: +301-480-3834.

E-mail address: [ss1@nih.gov](mailto:ss1@nih.gov) (S. Subramaniam).

structures where the nominal resolution is in the vicinity of 10 Å or better, it is also possible to explore refinement procedures that take into account possible differences in conformation of the sub-components between their isolated and complexed states.

Although obtaining near-atomic resolution maps remains an ultimate goal for imaging in some cases (Henderson, 1995; van Heel et al., 2000), a large number of single particle imaging efforts have as their target, the determination of density envelopes at intermediate (~7–10 Å) resolution. These latter cases include structurally heterogeneous and dynamic protein assemblies where the structural variation between individual, isolated molecular assemblies provides an upper limit to the resolution that can be attained, as well as structurally homogeneous multi-protein complexes where medium resolution density maps provide sufficient detail to dock known atomic structures of the sub-components previously determined by crystallographic or NMR methods. It is clear that significant increases in the speed of structure determination at such medium resolution could result from the implementation of effective schemes for automation. In principle, automation can be envisioned for almost all steps in the process, including specimen preparation, data acquisition, image selection, structure refinement, and docking of the X-ray coordinates into the density map, and some level of progress has been achieved in each of these instances (Carragher et al., 2000; Fellmann et al., 2002; Ludtke et al., 1999; Rossmann et al., 2001; Volkman and Hanein, 1999; Wu et al., 2003; Zhang et al., 2001). In the present work, we focus on advances in digital imaging technology that can eliminate the time that is spent on processing and digitizing images recorded on photographic film. Despite impressive improvements in CCD detector technology, commercially available 2K × 2K CCD cameras are not suitable for structural studies at resolutions better than ~15 Å (Faruqi and Subramaniam, 2000). The availability of digital data acquisition devices with performance comparable to photographic film is therefore highly desirable, and indeed essential, for continued success in implementing enhanced levels of automation in structure determination.

In this work, we describe the performance of a new generation of 4K × 4K CCD detectors at 120 kV for use in electron microscopic applications, and associated improvements in automation of structure determination. The camera assembly includes improvements in the phosphor, the optical fiber used to couple the phosphor to the CCD, and in the bonding of the fiber to the phosphor and to the CCD. We report on the use of this camera for single particle electron microscopic applications, and demonstrate that its performance is comparable to film for medium resolution cryo electron microscopic applications.

## 2. Methods

### 2.1. Sample preparation

Samples of purified icosahedral E2 catalytic domain (E2CD) of the *Bacillus stearothermophilus* pyruvate dehydrogenase, at 3 mg/ml concentration in 50 mM sodium phosphate buffer, pH 7.0, were prepared as described (Allen and Perham, 1997). Thick carbon films (150 Å) were evaporated onto Quantifoil R 2/4 template grids, and the grids were baked at 130 °C for 1 h, then soaked overnight in a covered glass petri dish filled with chloroform. In a cold-room environment (4 °C, 93% humidity), 3 µl of a solution containing 150 µg/ml of purified E2CD and 50 mM sodium phosphate buffer was deposited on each grid. Blotting and freezing in liquid ethane cooled by liquid nitrogen was carried out using a cryoplunge apparatus (GATAN, PA).

### 2.2. CCD camera

The new CCD camera (the Gatan Ultrascan 4000SP) is similar to existing CCD cameras for electron microscopy (Daberkow et al., 1996; Krivanek and Mooney, 1993) in that it consists of a scintillator optically coupled to a scientific-grade CCD by a fused fiber-optic plate. This camera differs from earlier versions in a number of details in the optical coupling, the phosphor deposition method, the overcoating, the fiber-optic plate, the fiber attachment process and in the pixel size. A reduced phosphor thickness decreases the lateral extent of the electron-scintillator interaction volume and with the other changes gives a significant reduction in light-leak from one pixel to the next. The improved electron and optical resolution allows the use of a smaller pixel size. The camera has 15 µm pixels in an area of 61 × 61 mm<sup>2</sup> yielding a total of 4K × 4K pixels. The conversion efficiency of the CCD camera was measured to be 1.37 counts/ primary electron, and the readout noise in a dark-subtracted image was 0.8 primary electrons.

### 2.3. Electron microscopy

Images were recorded either on SO-163 electron image film (Eastman Kodak, Rochester, NY) or the CCD camera mounted on a Tecnai2 electron microscope (FEI, OR) operating at 120 kV, equipped with either a tungsten or LaB6 filament. For film images, the exposed films were developed for 12 min in full-strength D19 developer. Digitization was carried out with a flat-bed Zeiss SCAI scanner (Z/I Imaging, Huntsville, AL) using a step size of 7 µm. The resolution tests with the graphite fringes were carried out both on a Tecnai 12 and a Tecnai 20 microscope operating at 120 kV with identical results. The initial characterization of the camera was carried out at GATAN Inc. on a Tecnai 20 microscope

operating at 120 kV using a LaB6 filament, producing the data shown in Fig. 2. These results were confirmed upon installation at NIH on the Tecnai 12 microscope operating at 120 kV equipped with a LaB6 filament. Due to technical difficulties in operating the Tecnai 12 stably using a LaB6 filament, all of the subsequent work reported here was carried out using a tungsten filament.

For experiments involving quantitative comparisons of CCD and film, images were recorded in the presence or absence of a film of amorphous carbon at room temperature. The images were recorded at the same underfocus value, and the same area of the specimen was used to ensure equal image contrast. Film images were acquired using a nominal magnification of 67 000 $\times$ , and digitized onto 7  $\mu\text{m}$  pixels yielding a pixel size of 1.04  $\text{\AA}$ . CCD images were acquired using the same nominal magnification, but correspond effectively to a magnification of 89 700 in the plane of CCD because of the post-magnification ratio 1.34 $\times$ . Each CCD pixel thus corresponds effectively to 1.67  $\text{\AA}$  in the specimen plane. Images were alternately recorded on film and CCD with illumination and exposure times held constant in order to ensure equal doses at the specimen. Consistent results were also obtained from CCD images acquired using a nominal magnification of 110 000 $\times$  at which the effective CCD pixel size (1.02  $\text{\AA}$ ) is nearly equal to the film pixel size. For CCD images, gain normalization was carried out following subtraction of the dark background signal. Images from film and CCD were calibrated in terms of primary electrons per pixel before further analysis in order to allow meaningful comparison of power spectra (see below). The CCD camera conversion efficiency was calibrated using a Faraday cup. Images of E2CD molecules were acquired on CCD using a nominal magnification of 67 000 $\times$ , with an electron dose about 20  $\text{el}/\text{\AA}^2$ , and at a range of underfocus values (2–3  $\mu\text{m}$ ).

#### 2.4. Measurement of ice thickness

Ice thickness was estimated using previously reported methods (Lepault et al., 1983; Zhang et al., 2001) based on the optical densities of images acquired from the central regions (0.6  $\mu\text{m}$  wide) of the hole and a reference image of an empty hole, using the equation

$$t = k \log(I_{\text{ref}}/I_{\text{ice}}),$$

where  $t$  is the thickness,  $k$  is a proportionality constant, and  $I$  is the average intensity of each CCD image, which is proportional to the optical density. For the Tecnai 12 microscope operating at 120 kV with a 40  $\mu\text{m}$  objective aperture, we use a  $k$  value of  $\sim 7500 \text{\AA}$  for the ice thickness measurements. A cryo electron tomogram (data not shown) was made from the same region used for the optical density measure-

ment, suggesting the ice thickness measurement is accurate to within  $\sim 15\%$ .

#### 2.5. Manual vs. automated particle selection

We employed both manual and automated methods for particle selection from images. While the three-dimensional model we report here is from a data set using manually selected particles, we have investigated the potential of automated selection approaches using the program BOXER (EMAN suite (Ludtke et al., 1999)) invoked on a GNU/Linux workstation, and report briefly on our findings in this section. The micrographs, in CCP4 format, were opened in BOXER with the box size selected to snugly fit the size of the particles and representative views were selected. The option “Process $\rightarrow$ Autobox” was then used to automatically identify particles in an area covering 2048  $\times$  2048 pixels. Selection parameters were adjusted to obtain the best selection of particles while minimizing noise, and automated selection was then initiated. The boxed data files produced by BOXER were converted to coordinate lists that could be read in the MRC program LABEL using a simple Perl script. In general, many more particles were selected by the automated process, and the set included  $>50\%$  of those selected manually by an experienced user. Variations between manual and automated processes were mainly related to variations in ice thickness between the center and the outer edges, which is often the case in vitrified specimens. Although the automated selection process does result in selection of a higher fraction of candidate molecular images in a given area, and includes particles of questionable quality, these are easily discarded at a later stage in the processing based on setting suitable thresholds such as phase residual cutoffs (Grigorieff, 1998) for particles used for reconstructing the three-dimensional model. Overall, our results suggest that the performance of BOXER, even in its present implementation, is useful for rapid selection of molecular images.

#### 2.6. Image processing and generation of three-dimensional models

Construction of an initial model and its subsequent refinement was carried out essentially as documented in Milne et al. (Milne et al., 2002). Refinement of the initial model constructed in the context of IMAGIC (van Heel et al., 1996) was carried out in a GNU/Linux cluster of Pentium class computers. An improved version of the program FREALIGN (v. 5.02) (Grigorieff, 1998), kindly provided by Dr. Richard Henderson (Laboratory of Molecular Biology, MRC, Cambridge, UK), was used to refine the values for orientational parameters of projections of individual E2CD complex particles relative to the previously constructed initial model.

## 2.7. Generation of X-ray map and projections

The program PDBBLUR in the SITUS package (Wriggers et al., 1999) was used to generate density maps based on the coordinates of the X-ray structure of the icosahedral E2CD complex (PDB ID: 1B5S) using a temperature factor of  $2000 \text{ \AA}^2$ . We selected a voxel size ( $3.15 \text{ \AA}$ ), similar to that of experimentally obtained electron microscopic maps ( $3.34 \text{ \AA}$  with  $2 \times 2$  binned data). A Gaussian smoothing kernel was used with correction for lattice interpolation smoothing effects and with a scaling factor of one. The program CONFORMAT was used to convert the resulting maps from SITUS into CCP4 format, and the EMAN program PROJECT3D was used to project electron density maps along the 2-, 3-, and 5-fold symmetry axes of the icosahedral complex.

## 3. Results

### 3.1. An improved AutoEM interface

AutoEM is a collection of programs that implements semi-automated low-dose image acquisition procedures on a Tecnai 12 electron microscope using the scripting functionality available on the microscope computer (Zhang et al., 2001). Although AutoEM supports data acquisition at different levels of automation, we use it most frequently at the lowest level of automation, where the user first manually selects regions of interest that are to be imaged. All subsequent steps of image acquisition are then carried out automatically to record low-dose images on either film or CCD, at desired defocus values, and under conditions that satisfy user-specified limits for drift rates of the specimen stage. The present appearance of the user interface is shown in Fig. 1. Improvements over the previously reported version include: (i) inclusion of an option to automatically record and transfer all parameters related to data acquisition into a database used for structure determination and refinement, (ii) inclusion of procedures to automatically record a small image of the carbon area near the imaged hole, which could be used to provide an independent estimate for defocus parameters in cases where low particle density in the hole makes determination of the phase contrast transfer function (CTF) difficult, and (iii) improved background subtraction and gain normalization procedures optimized for use in conjunction with the  $4K \times 4K$  CCD camera.

### 3.2. Performance of the 4K CCD camera

The design parameters for CCD cameras used for cryo electron microscopic applications reflect a compromise between several conflicting requirements: the

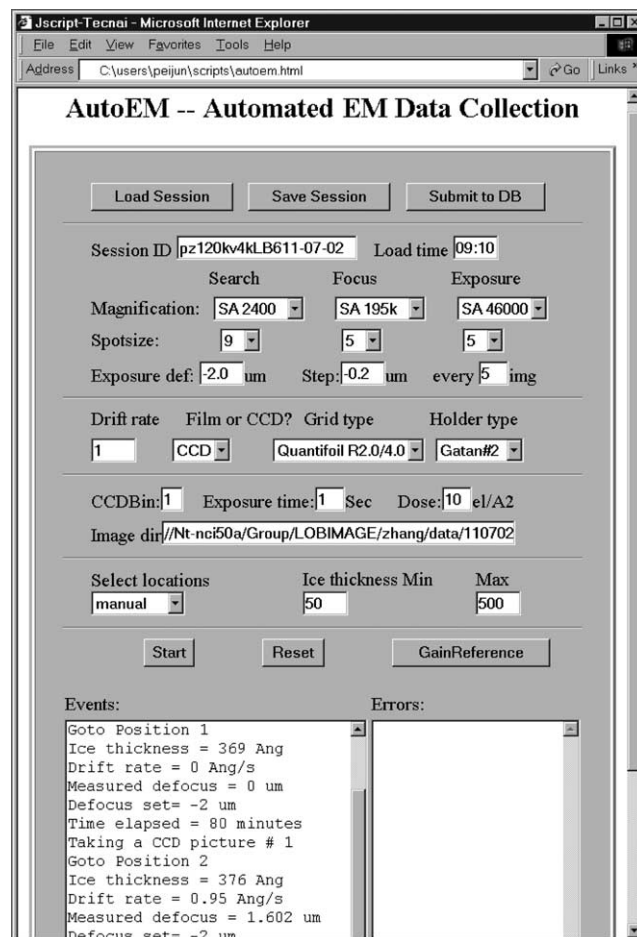


Fig. 1. An improved AutoEM user interface for automated data collection. To initiate data collection on film or the CCD, key parameters such as electron dose, exposure time, magnification, spot size, defocus values, acceptable specimen ice thickness, and acceptable specimen drift rates can be either set by the user, or default values from the previous run can be retained. The actual values of these parameters for each image, as well as much of the information associated with a particular experiment including session ID, grid type, holder type, or specimen loading time can be sent directly to a central database by activating the “Submit to DB” option. To improve the gain correction of acquired images in Tecnai Imaging Analysis software (TIA), a gain reference preparation routine also has been implemented into the user interface.

use of sufficiently large pixel sizes to obtain “near-independent” pixels, yet small enough that the camera can be used for imaging at low magnification to keep the electron dose at the specimen to a minimum, the use of a phosphor with high sensitivity in order to get a sufficiently high signal at the low doses used in cryo electron microscopy, yet thin enough to minimize the spread of the incident electron and secondary photons over pixels in the detector plane. We first address the issue of maximum resolution attainable by the camera when electron dose is not a limiting factor. Fig. 2 shows images of graphite recorded on a Tecnai 20 microscope operating at 120 kV with a LaB<sub>6</sub> filament, and the cor-

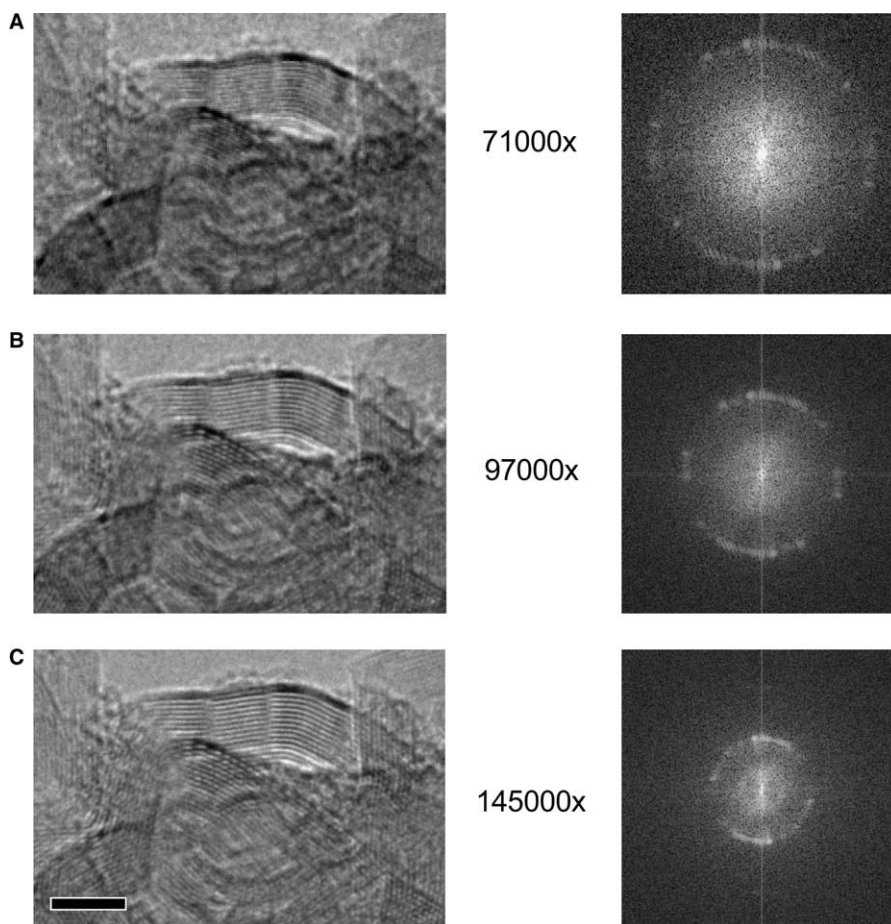


Fig. 2. Evaluation of the  $4K \times 4K$  CCD camera. Images of graphitized carbon images were recorded on the CCD at nominal magnifications of 71 000 $\times$ , 97 000 $\times$ , and 145 000 $\times$  (left panels) at doses of 122, 332, and 568  $e/\text{\AA}^2$  at 120 kV using a LaB6 filament. The corresponding Fourier transform ( $256 \times 256$ ) of each image is shown on the right.

responding Fourier transforms. Identical results were obtained with a Tecnai 12 microscope operating under the same conditions. The magnifications shown correspond to the nominal magnifications on the film plane, the actual magnification is  $1.4\times$  higher in the CCD plane (instead of  $1.34\times$  for the Tecnai 12 microscope used for the rest of the data presented here). Graphite fringes are clearly visible in the image even at 71 000 $\times$ . At this magnification, each  $15\ \mu\text{m}$  pixel corresponds to  $\sim 1.5\ \text{\AA}$  in the specimen plane, and the edge of the power spectrum thus corresponds to a spatial frequency of  $\sim 3\ \text{\AA}$ . The Fourier transforms show that the  $3.4\ \text{\AA}$  graphite reflections are visible in the images recorded at all three magnifications. The lowest magnification used (71 000 $\times$ ) is close to the values used typically in low-dose applications. The graphite fringes are not evident in images recorded at magnifications lower than 71 000 $\times$  (data not shown), but this is not surprising since the spacing of the fringes is already very close to the Nyquist frequency at 71 000 $\times$  (Fig. 2A).

While the visibility of graphite fringes in Fourier space is a useful way to demonstrate that meaningful signal to

noise exists on a detector at a given frequency, it is not the best method for quantitatively comparing the performance of two or more image acquisition media. From one graphite exposure to the next, alignment of fringes to the pixels can change, altering the contrast, especially at high spatial frequencies. Further, the microscope phase contrast transfer function (CTF) may be affected slightly by magnification changes, resulting in fringes coming in and out of focus in an uncontrolled manner during a magnification series. Finally, image rotation between magnifications can also affect contrast against the square CCD pixel array. In general, it would be desirable for a specimen to be used for resolution studies to be spatially uniform, isotropic and contain contrast variations equally distributed across all spatial frequencies. Amorphous carbon films are excellent test specimens for this purpose because they meet these criteria. Frequency-dependent variations in the amplitude of the power spectrum obtain from amorphous carbon images can be attributed solely to the effect of the phase contrast transfer function of the microscope and the limitations imposed by the transfer function of the detector.

In Fig. 3A, we show the Fourier transform of an image recorded from amorphous carbon at 120 kV, recorded at an underfocus of  $\sim 0.5 \mu\text{m}$ . The highest resolution at which the Thon ring fringes are visible in the image is  $\sim 4.2 \text{ \AA}$ , as also illustrated in a plot of the radially averaged power spectrum (Fig. 3B). This resolution is limited primarily by the coherence of the LaB<sub>6</sub> filament used for the experimental measurements (see

below), and provides a measure of the resolution performance attainable with the new 4K CCD detector for operation at 120 kV.

Comparison of the Thon ring profile of images recorded on film or CCD under identical electron optical conditions provides a more incisive test of the performance of the CCD camera. Carbon images were recorded on a Tecnai 12 microscope equipped with a

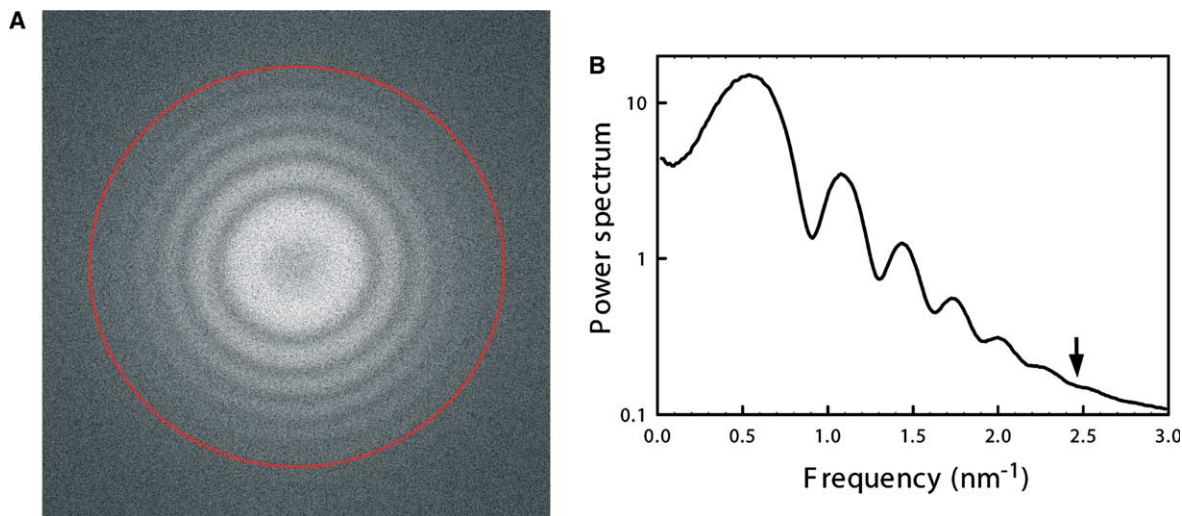


Fig. 3. Thon rings in the CCD images. (A) Fourier transform of an image of amorphous carbon taken on the  $4K \times 4K$  CCD camera at a nominal magnification of  $67\,000\times$ . The red circle indicates the highest resolution ( $4.2 \text{ \AA}$ ) at which Thon rings can be visualized. (B) The power spectrum of the same amorphous carbon image with the  $4.2 \text{ \AA}$  resolution peak indicated (arrow).

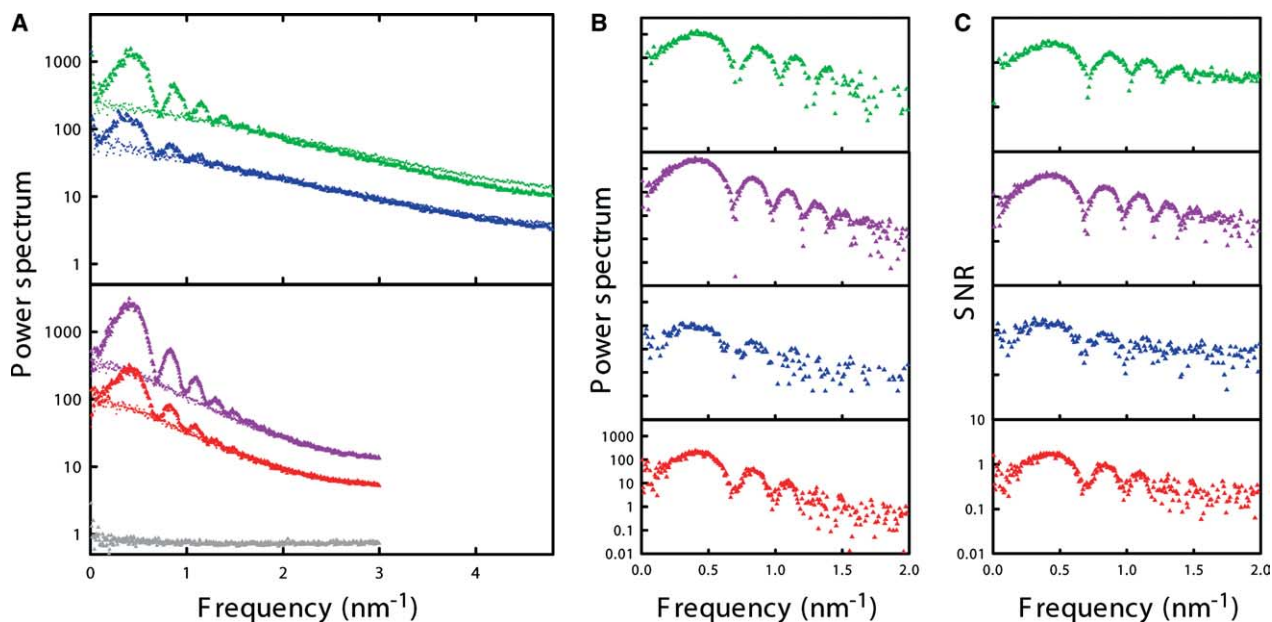


Fig. 4. Power spectra and analysis from CCD and digitized film images. (A) Power spectra from amorphous carbon images taken with CCD (red and pink/purple, lower panel) and film (blue and green, upper panel) under similar electron optical conditions, similar defocus values ( $\sim 0.6 \mu\text{m}$ ), and at electron dose levels of  $56 \text{ el/\AA}^2$  (pink/purple and green) or  $17 \text{ el/\AA}^2$  (red and blue). The dotted lines are power spectra derived from images collected without specimen, while the gray line is the power spectrum of a dark image collected on the CCD. Film images were digitized at  $7 \mu\text{m}/\text{pixel}$ . The Nyquist frequency is  $4.8 \text{ nm}^{-1}$  for film images and  $3 \text{ nm}^{-1}$  for CCD images. (B, C) Comparison of the difference power spectra (B) and signal to noise ratio (SNR) (C) between film images (green and blue) and CCD images (pink/purple and red) recorded at electron dose levels of  $56 \text{ el/\AA}^2$  (pink/purple and green) and  $17 \text{ el/\AA}^2$  (red and blue).

tungsten filament under identical electron optical conditions and with identical electron doses either on the  $4K \times 4K$  CCD, or on SO-163 film and digitized with a Zeiss scanner using the smallest step size available ( $7\mu\text{m}$ ). Comparison of power spectra (Fig. 4A) at two different electron doses ( $17\text{el}/\text{\AA}^2$ ) and ( $55\text{el}/\text{\AA}^2$ ) demonstrates that the quality of the images recorded with the CCD camera are easily comparable to, if not better than, the digitized film images. The power spectra reported here were obtained by rotationally averaging the squared moduli of normalized fast Fourier transforms of the images. The image signal from the power spectrum of amorphous carbon increases as the square of the dose while the signal corresponding to the power spectrum obtained with uniform illumination (i.e., without carbon) increases linearly with the dose. Peaks in the power spectrum are visible to resolution of  $\sim 7\text{\AA}$  in the case of both the film and CCD images. The power spectrum has contributions both from the coherence

envelope of the illumination as well the intrinsic power spectrum of the carbon film following its modification by the microscope phase contrast transfer function. At frequencies where there is complete loss of contrast, the value of the power spectrum must equal the value measured in the absence of the specimen as is indeed observed (Fig. 4A).

To obtain a more quantitative comparison, it is possible to calculate a signal-to-noise ratio (SNR) from the dose pairs. Since signal and noise power are statistically independent, they add simply and hence signal power can be obtained by subtracting noise power from total power of the amorphous carbon images, as shown in Fig. 4B. Alternatively, the uniform illumination images can be also used as “noise” images subject to the following correction. A small loss in average signal can occur due to elastic scattering for the amorphous carbon images. At high spatial frequency where there is no specimen contrast, this difference can be measured by taking the ratio of the curves only in that region. If the entire uniform illumination power spectrum is reduced by that ratio, it can be used as the effective noise in the specimen image. It is also possible to use the bottom envelope of the Thon rings pattern variation for this purpose, but the power spectrum near the zeros is very noisy so this method is considered less reliable. The

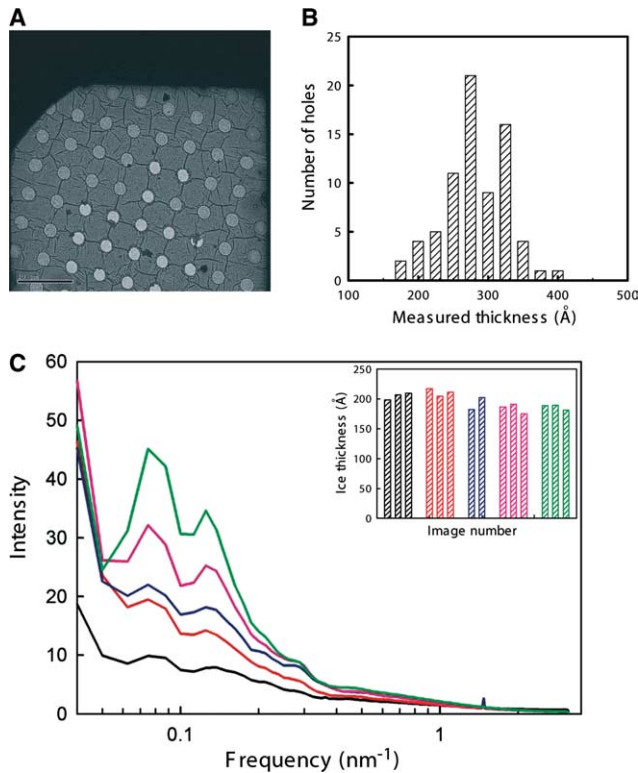


Fig. 5. Ice thickness measurements and dose titration experiments. (A) Low magnification ( $470\times$ ) image of E2CD on a R2/4 Quantifoil grid. (B) Distribution of the central ice thickness of 100 holes, measured in AutoEM using the image of an area  $\sim 0.6\mu\text{m}$  wide in the center of the hole. (C) Averaged power spectra from CCD images of E2CD taken at a nominal magnification of  $67000\times$  at electron doses of  $10\text{el}/\text{\AA}^2$  (black),  $20\text{el}/\text{\AA}^2$  (red),  $30\text{el}/\text{\AA}^2$  (blue),  $40\text{el}/\text{\AA}^2$  (pink), and  $50\text{el}/\text{\AA}^2$  (green). Inset: ice thickness measurement on the holes where the images were recorded. The same color scheme is used to indicate electron dose levels of 10, 20, 30, 40 or  $50\text{el}/\text{\AA}^2$ , respectively. The curves suggest that a dose of about  $20\text{el}/\text{\AA}^2$  is a reasonable compromise between preserving the information at higher frequencies, while providing adequate signal-to-noise ratios for detecting molecules in the image.

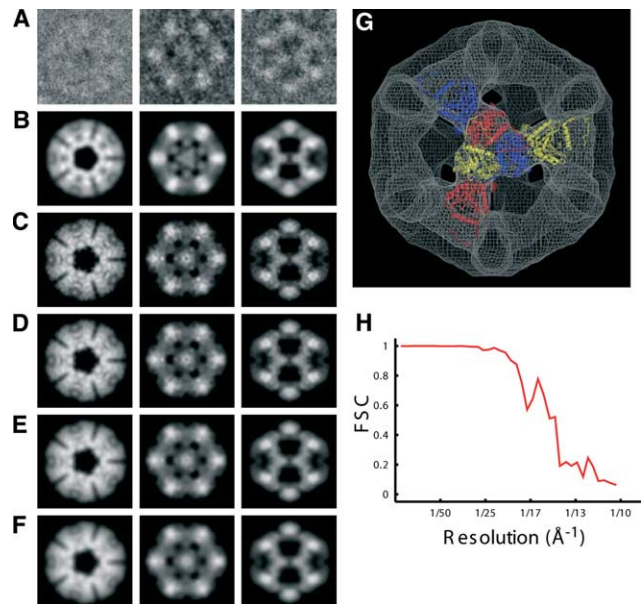


Fig. 6. Construction and evaluation of a three-dimensional model for E2CD. (A) Filtered images of individual particles corresponding roughly to views along 5-, 3-, and 2-fold axes of the icosahedron. (B) Projections along the 5-, 3-, and 2-fold axes from the three-dimensional model constructed using 2000 molecular images. (C–F) Projections from map calculated from the X-ray structure of E2CD at 12, 15, 18, and  $21\text{\AA}$ , respectively. (G) Superposition of map and co-ordinates. (H) Fourier shell correlation (FSC) plot comparing randomly divided halves of the data set. The correlation coefficient is 0.5 at  $\sim 15\text{\AA}$ .

SNR is then calculated from the total power ( $T$ ), and the noise power ( $N$ ) as follows:

$$\text{SNR} = (T - N)/N.$$

It is useful to note that if only a measure of the SNR, but not the absolute power spectrum is required, it is not necessary to calibrate the detectors in absolute terms, such as number of primary electrons per pixel since the calibrations cancel in the ratio above. Consistent with the other measures of performance, the data in Fig. 4C demonstrate that the signal-to-noise ratios of the CCD detector are as good as that of digitized film throughout the indicated frequency range.

A measure of the “fog” level of the CCD camera is also presented in Fig. 4A. For the CCD camera, the differences between pairs of dark reference images provide a measure of the total readout noise, and the fog level would correspond to the square root of two times the readout noise. The power spectrum of this two-image readout noise is shown in Fig. 4A. The fog level power spectrum of film could not be obtained due to range restrictions in the scanner so no direct comparison with film is presented. Note that there is room for another factor of 3–5 reduction in dose on the CCD before the fog level would be expected to affect the power spectrum in the high spatial frequency range and perhaps a factor of 10 before the readout noise would affect the noise power in the spatial frequency range with significant signal power.

### 3.3. Ice thickness measurement

The test studies with the carbon films suggest that the 4K × 4K CCD camera can perform as well as digitized film both in terms of signal-to-noise ratios and the resolution that is achievable. As a direct evaluation of the potential of the camera in a biological application, we have evaluated its use for biological structure determination using a test specimen, the icosahedral E2 catalytic core complex of the *B. stearothermophilus* pyruvate dehydrogenase (Milne et al., 2002; Perham, 1991). Figs. 5 and 6 present different aspects of this analysis, as described in greater detail below.

First, we present the use of the CCD camera to generate overview images (Fig. 5A) at low magnification (~470×) to provide an assessment of the distribution of ice thickness in different regions of the specimen. AutoEM uses measurements of the optical density of holes covered with vitreous ice to calculate the local ice thickness at each location, and proceeds with image collection only when the thickness falls within the range specified by the user at the beginning of data collection. In a good specimen, a significant fraction of holes are covered with ice (Fig. 5A). An interesting finding from our analysis of frozen hydrated specimens is that there is a sufficiently broad intrinsic variation in ice thickness

(Fig. 5B) produced under standard blotting conditions. AutoEM records this parameter for use in later processing steps to distinguish the ranges of ice thickness that result in the best images for a given specimen. Once holes with the correct thickness have been selected, images can be acquired over a range of doses. As discussed below, the ice thickness measurements have also been important in helping establish criteria for electron dosage for imaging.

The amorphous power spectra in Fig. 4 with images of amorphous carbon film demonstrate that the performance of the CCD is comparable to film under low dose illumination conditions. In Fig. 5C we show power spectra arising only from the protein molecules in the hole over a range of doses from 10 to 50 e/Å<sup>2</sup>. The spectra show that the power spectrum profile of the pyruvate dehydrogenase complex can be recognized even with the images recorded at 10 e/Å<sup>2</sup>. At doses above 30 e/Å<sup>2</sup>, the increase in signal at lower spatial frequencies is not matched by proportional increases at the higher spatial frequencies, consistent with the expectation of the increasing extent of radiation-induced specimen damage. A dose of 20 e/Å<sup>2</sup> is thus a reasonable compromise between minimizing radiation damage while maximizing the signal strength in the image. The trends in Fig. 5C showing the effect of varying electron doses are not due to systematic variations in ice thickness, since all images used have approximately the same average ice thickness (Fig. 5C inset).

### 3.4. Three-dimensional model constructed from CCD data

We have used 2000 manually selected images of E2CD recorded at doses of ~20 e/Å<sup>2</sup> to determine a three-dimensional model for the structure of this protein complex using procedures described previously (Milne et al., 2002). Selected individual images (Fig. 6A), although noisy, clearly show the features characteristic of the views of the complex along the 5-, 3-, and 2-fold icosahedral axes. The reprojections from the final three-dimensional model along the same directions are presented in Fig. 6B. The nominal resolution of the model is about 15 Å (Fig. 6H), and is almost exactly the same as the resolution of a model constructed from a similar set of images recorded on film (Milne et al., 2002). Verification that the model correctly reflects the general structural features of the complex is presented in panels c–e of Fig. 6, which shows projections from maps at different resolutions calculated using a 4.5 Å model for the structure derived from X-ray crystallography. The model generated with the images recorded on the CCD displays features roughly most consistent with the reprojections at 15 and 18 Å (Figs. 6D and E). The agreement between the experimentally density map with the atomic coordinates is also evident from the superposition of the map and the atomic co-ordinates (Fig. 6G).

#### 4. Discussion

With the increasing interest in understanding the structures of large macromolecular assemblies, it is important to have tools for electronic data collection that circumvent the slow and manual processing of images recorded on photographic film. CCD detectors are already used routinely in a number of important biological applications such as tomography of cellular organelles (Dierksen et al., 1995; Koster et al., 1992), where the resolution requirements are relatively modest. In contrast, for electron imaging applications where the goal of the microscopy is to obtain structural information at near-atomic resolution, photographic film continues to remain the medium of choice. Applications involving structure determination of large multi-protein complexes often have resolution requirements that fall in an intermediate range, where the goal of the imaging is to arrive at three-dimensional envelopes typically at 10–15 Å resolution. Here, we present evidence that for such medium resolution requirements, the performance of a new generation of 4K × 4K CCD detectors is easily comparable to that of film digitized with the Zeiss PHODIS scanner.

The success of CCD detectors for electron microscopy is based on a number of factors, which include its fast response, low noise electronics, and potential for automation. In the present camera, the sensitivity of the phosphor has allowed the recording of images with sufficient contrast at electron doses between 15 and 20 el/Å<sup>2</sup>. This is acceptable for a number of low-dose applications, although advances towards the lowest possible dose at which there is adequate contrast are clearly desirable. Our experience is that even at doses as low as 10 el/Å<sup>2</sup>, the signal per pixel (i.e., number of counts) is well above the readout noise, as indeed reflected in the power spectrum shown in Fig. 4. However, further improvements are required for useful images to be collected at doses in the range of 5–10 el/Å<sup>2</sup>. Since the readout noise in a dark-subtracted image is 0.8 electrons in this camera, this source of noise is unimportant for doses down to a few primary electrons per pixel. One may therefore expect that the bulk of improvement needed in the 5–10 el/Å<sup>2</sup> range is likely to come from proportional reductions in the noise contributed by scintillator and image transfer processes.

In almost all phosphor-based CCD cameras currently used for electron microscopic applications, the loss of resolution at higher spatial frequencies is caused by the spread of incoming electrons in the phosphor layer and the underlying fiber optic plate (Downing and Hendrickson, 1999) and by the spread of the emitted light photons in the phosphor layer (Daberkow et al., 1991; Faruqi and Tyrell, 1999). The extent of this spread can be quantitatively analyzed by inspection of the modulation transfer function (MTF), which is the Fourier

transform of the point spread function, which essentially reports on the attenuation of different spatial frequencies present in the input signal. At lower voltages, the optical spread dominates, while at higher voltages, the electron spread dominates with the break-even voltage determined by phosphor thickness and fiber optic plate composition. The net value of the MTF at the higher frequencies declines with increasing voltage, and this poses a major problem in designing CCD cameras suitable for high resolution at higher voltages. However, significant improvements can be expected from progressive improvements in phosphor composition, bonding technology, and alternative ways of constructing the photon image transfer mechanism. Replacing the fiber-optic plate with a non-contact lens-based optical coupling offers the promise of reduced scintillation noise through the elimination of electron backscatter but at the cost of lower light transmission efficiency (Mooney and Krivanek, 1994). The use of a decelerator built into the microscope column below the objective lens has also been proposed as a way to circumvent the poor performance of CCD cameras at high voltages (Downing et al., 2000). In principle, it is also possible to eliminate the phosphor layer altogether, and use the CCD as a direct electron detector. This idea has been implemented in hybrid pixel detectors, and the evaluation of a detector with 64 × 64 pixels has been recently reported (Faruqi et al., 2003). These alternative technologies are in the early stages of development, although they have the potential to be incorporated into future designs for detectors used in biological electron microscopy. For the present, our findings with the 4K × 4K CCD camera suggest that the improvements in phosphor-based fiber-optic coupled cameras, and related technologies offer promising avenues for further immediate advances in the use of digital detectors for high resolution, low-dose biological electron microscopy.

#### References

- Allen, M.D., Perham, R.N., 1997. The catalytic domain of dihydrolipoyl acetyltransferase from the pyruvate dehydrogenase multienzyme complex of *Bacillus stearothermophilus*. Expression, purification and reversible denaturation. *FEBS Lett.* 413, 339–343.
- Carragher, B., Kisseberth, N., Kriegman, D., Milligan, R.A., Potter, C.S., Pulokas, J., Reilein, A., 2000. Leginon: An automated system for acquisition of images from vitreous ice specimens. *J. Struct. Biol.* 132, 33–45.
- Conway, J.F., Wikoff, W.R., Cheng, N., Duda, R.L., Hendrix, R.W., Johnson, J.E., Steven, A.C., 2001. Virus maturation involving large subunit rotations and local refolding. *Science* 292, 744–748.
- Daberkow, I., Herrmann, K.H., Liu, L., Rau, W.D., Tietz, H., 1996. Development and performance of a fast fibre-plate coupled CCD camera at medium energy and image processing system for electron holography. *Ultramicroscopy* 64, 35–48.
- Daberkow, I., Herrmann, K.H., Liu, L.B., Rau, W.D., 1991. Performance of electron image converters with Yag single-crystal screen and CCD sensor. *Ultramicroscopy* 38, 215–223.

- Dierksen, K., Typke, D., Hegerl, R., Walz, J., Sackmann, E., Baumeister, W., 1995. Three-dimensional structure of lipid vesicles embedded in vitreous ice and investigated by automated electron tomography. *Biophys. J.* 68, 1416–1422.
- Downing, K.H., Favia, P., Mooney, P.E., 2000. Electron decelerator for improved CCD performance in intermediate voltage electron microscopy. *Proceedings of the 58th Annual Meeting of the Microscopy Society of America*, pp. 734–735.
- Downing, K.H., Hendrickson, F.M., 1999. Performance of a 2k CCD camera designed for electron crystallography at 400 kV. *Ultramicroscopy* 75, 215–233.
- Faruqi, A.R., Cattermole, D.M., Henderson, R., Mikulec, B., Raeburn, C., 2003. Evaluation of a hybrid pixel detector for electron microscopy. *Ultramicroscopy* 94, 263–276.
- Faruqi, A.R., Subramaniam, S., 2000. CCD detectors in high-resolution biological electron microscopy. *Q. Rev. Biophys.* 33, 1–27.
- Faruqi, A.R., Tyrell, G.C., 1999. Evaluation of gadolinium oxysulphide (P43) phosphor used in CCD detectors for electron microscopy. *Ultramicroscopy* 76, 69–75.
- Fellmann, D., Pulokas, J., Milligan, R.A., Carragher, B., Potter, C.S., 2002. A relational database for cryoEM: experience at one year and 50,000 images. *J. Struct. Biol.* 137, 273–282.
- Frank, J., 1996. *Three-dimensional Electron Microscopy of Macromolecular Assemblies*. Academic Press, San Diego.
- Grigorieff, N., 1998. Three-dimensional structure of bovine NADH:ubiquinone oxidoreductase (complex I) at 22 Å in ice. *J. Mol. Biol.* 277, 1033–1046.
- Henderson, R., 1995. The potential and limitations of neutrons, electrons and X-rays for atomic resolution microscopy of unstained biological molecules. *Q. Rev. Biophys.* 28, 171–193.
- Jiang, W., Li, Z., Zhang, Z., Baker, M.L., Prevelige Jr., P.E., Chiu, W., 2003. Coat protein fold and maturation transition of bacteriophage P22 seen at subnanometer resolutions. *Nat. Struct. Biol.* 10, 131–135.
- Koster, A.J., Chen, H., Sedat, J.W., Agard, D.A., 1992. Automated microscopy for electron tomography. *Ultramicroscopy* 46, 207–227.
- Krivanek, O.L., Mooney, P.E., 1993. Applications of slow-scan Ccd cameras in transmission electron-microscopy. *Ultramicroscopy* 49, 95–108.
- Lepault, J., Booy, F.P., Dubochet, J., 1983. Electron microscopy of frozen biological suspensions. *J. Microsc.* 129, 89–102.
- Ludtke, S.J., Baldwin, P.R., Chiu, W., 1999. EMAN: semiautomated software for high-resolution single-particle reconstructions. *J. Struct. Biol.* 128, 82–97.
- Milne, J.L., Shi, D., Rosenthal, P.B., Sunshine, J.S., Domingo, G.J., Wu, X., Brooks, B.R., Perham, R.N., Henderson, R., Subramaniam, S., 2002. Molecular architecture and mechanism of an icosahedral pyruvate dehydrogenase complex: a multifunctional catalytic machine. *EMBO J.* 21, 5587–5598.
- Mooney, P.E., Krivanek, O.L., 1994. Image-coupling methods in CCD cameras for electron microscopy. *Proceedings of the 52nd Annual Meeting of the Microscopy Society of America*, pp. 406–407.
- Perham, R.N., 1991. Domains, motifs, and linkers in 2-oxo acid dehydrogenase multienzyme complexes: a paradigm in the design of a multifunctional protein. *Biochemistry* 30, 8501–8512.
- Ranson, N.A., Farr, G.W., Roseman, A.M., Gowen, B., Fenton, W.A., Horwich, A.L., Saibil, H.R., 2001. ATP-bound states of GroEL captured by cryo-electron microscopy. *Cell* 107, 869–879.
- Rossmann, M.G., Bernal, R., Pletnev, S.V., 2001. Combining electron microscopy with X-ray crystallographic structures. *J. Struct. Biol.* 136, 190–200.
- Stark, H., Rodnina, M.V., Wieden, H.J., van Heel, M., Wintermeyer, W., 2000. Large-scale movement of elongation factor G and extensive conformational change of the ribosome during translocation. *Cell* 100, 301–309.
- van Heel, M., Gowen, B., Matadeen, R., Orlova, E.V., Finn, R., Pape, T., Cohen, D., Stark, H., Schmidt, R., Schatz, M., Patwardhan, A., 2000. Single-particle electron cryo-microscopy: towards atomic resolution. *Q. Rev. Biophys.* 33, 307–369.
- van Heel, M., Harauz, G., Orlova, E.V., 1996. A new generation of the IMAGIC image processing system. *J. Struct. Biol.* 116, 17–24.
- Volkman, N., Hanein, D., 1999. Quantitative fitting of atomic models into observed densities derived by electron microscopy. *J. Struct. Biol.* 125, 176–184.
- Wriggers, W., Milligan, R.A., McCammon, J.A., 1999. Situs: a package for docking crystal structures into low-resolution maps from electron microscopy. *J. Struct. Biol.* 125, 185–195.
- Wu, X., Milne, J.L.S., Borgnia, M.J., Rostapshov, A.V., Subramaniam, S., Brooks, B.R.U., 2003. A core-weighted fitting method for docking atomic structures into low-resolution maps: application to cryo-electron microscopy. *J. Struct. Biol.* 141, 63–76.
- Zhang, P., Beatty, A., Milne, J.L., Subramaniam, S., 2001. Automated data collection with a Tecnai 12 electron microscope: applications for molecular imaging by cryomicroscopy. *J. Struct. Biol.* 135, 251–261.